

Impacts of the Madden–Julian Oscillation on Australian Rainfall and Circulation

MATTHEW C. WHEELER AND HARRY H. HENDON

Centre for Australian Weather and Climate Research, Melbourne, Victoria, Australia

SAM CLELAND

Bureau of Meteorology, Darwin, Northern Territory, Australia

HOLGER MEINKE

Centre for Crop Systems Analysis, Wageningen University, Wageningen, Netherlands

ALEXIS DONALD

Queensland Centre for Climate Change Excellence, Toowoomba, Queensland, Australia

(Manuscript received 18 April 2008, in final form 15 September 2008)

ABSTRACT

Impacts of the Madden–Julian oscillation (MJO) on Australian rainfall and circulation are examined during all four seasons. The authors examine circulation anomalies and a number of different rainfall metrics, each composited contemporaneously for eight MJO phases derived from the real-time multivariate MJO index. Multiple rainfall metrics are examined to allow for greater relevance of the information for applications. The greatest rainfall impact of the MJO occurs in northern Australia in (austral) summer, although in every season rainfall impacts of various magnitude are found in most locations, associated with corresponding circulation anomalies. In northern Australia in all seasons except winter, the rainfall impact is explained by the direct influence of the MJO's tropical convective anomalies, while in winter a weaker and more localized signal in northern Australia appears to result from the modulation of the trade winds as they impinge upon the eastern coasts, especially in the northeast. In extratropical Australia, on the other hand, the occurrence of enhanced (suppressed) rainfall appears to result from induced upward (downward) motion within remotely forced extratropical lows (highs), and from anomalous low-level northerly (southerly) winds that transport moisture from the tropics. Induction of extratropical rainfall anomalies by remotely forced lows and highs appears to operate mostly in winter, whereas anomalous meridional moisture transport appears to operate mainly in the summer, autumn, and to some extent in the spring.

1. Introduction

The importance of intraseasonal variations of rainfall for agricultural production and decision making is becoming increasingly recognized (e.g., Webster and Hoyos 2004). For instance, intraseasonal rainfall variations, and especially break conditions, have a pronounced impact on Indian groundnut (peanut) production, which is one of the most economically important crops sown during the Indian monsoon (Gadgil et al.

1999). In a broader global context, Meinke and Stone (2005) highlighted numerous agricultural decisions that could be made given forecasts targeted to the intraseasonal time scale. These include logistical decisions for the scheduling of planting and harvest operations, maintenance works, and the application of fertilizers.

The economic importance of intraseasonal rainfall variations stems from the prominence of intraseasonal variance. In the tropics, and especially the monsoon regions, rainfall varies strongly on weekly to monthly time scales (e.g., Gadgil 2003; Webster et al. 1998; Wheeler and McBride 2005). Extratropical rainfall also exhibits pronounced intraseasonal variations. This is illustrated in Fig. 1, which shows time series of area-averaged rainfall for a tropical and extratropical region in Australia.

Corresponding author address: Dr. Matthew C. Wheeler, CAWCR, Bureau of Meteorology, GPO Box 1289, Melbourne, VIC 3001, Australia.
E-mail: m.wheeler@bom.gov.au

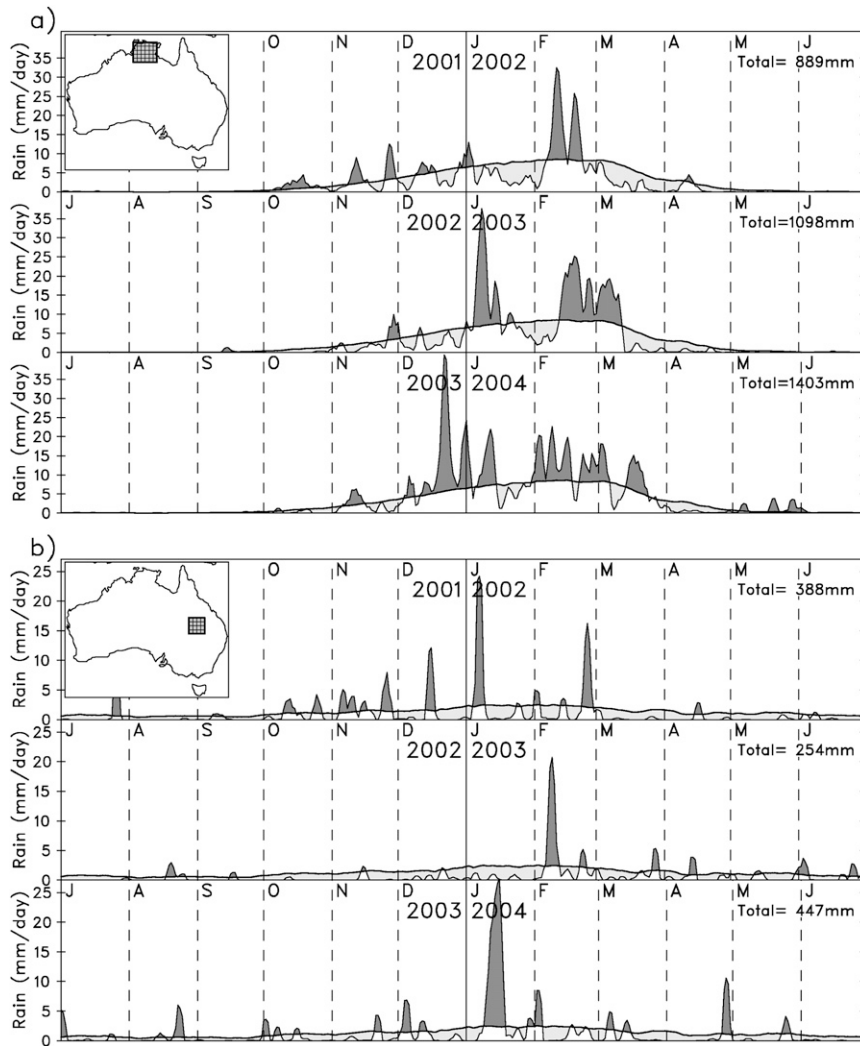


FIG. 1. Time series of 3-day running-mean rainfall (thin curves) for the period 1 Jul 2001 to 30 Jun 2004, area-averaged for (a) the Top End of Australia (12° – 17° S, 130° – 136° E); and (b) a region in eastern Australia (24° – 28° S, 144° – 148° E). Also shown are smoothed climatological annual cycles (thicker curves) in each region, computed using all daily data from 1948 to 2006. Positive rainfall anomalies with respect to the smoothed climatology are shaded dark. Each year is split at 1 Jul, and the yearly total rainfall for each July–June period is provided on the right of each yearly panel.

The tropical “Top-End” region (Fig. 1a) shows typical intraseasonal variability of monsoon rainfall: a wet season comprises several bursts of rainfall that are separated by breaks of comparatively reduced rainfall, each typically lasting 10–40 days. Similar intraseasonal variations are also observed in the more southern location in Fig. 1b. For example, January 2003 was predominantly dry, followed by a mostly wet February, and then followed by 2 weeks of dry conditions in early March.

A major source of intraseasonal rainfall variability, especially in the tropical Indo-Pacific region, is the Madden–Julian oscillation (MJO; Madden and Julian

1972; Zhang 2005). Direct impacts of the MJO on rainfall across the tropical Indo-Pacific have been widely documented, but the MJO also causes variations in weather in far-reaching extratropical locations around the globe (e.g., Jones 2000; Bond and Vecchi 2003; Carvalho et al. 2004; Barlow et al. 2005; Donald et al. 2006; Pohl et al. 2007). In fact, the MJO is considered to be a key source of mostly untapped predictability of subseasonal weather variations in both the tropics and extratropics (Schubert et al. 2002; Waliser 2005).

Here we consider in detail the component of Australian rainfall (both tropical and extratropical) that is

associated with the MJO, as it is this component that is likely most predictable on the intraseasonal time scale. We do this for each of four seasons, presenting information on MJO-induced changes in the mean and other aspects of the rainfall distribution, such as the occurrence of extreme events. These changes are interpreted in light of the associated changes in circulation, providing a greater physical understanding of the relationships shown. The results confirm the strong seasonality of the MJO's impact on rainfall and provide a basis for estimating the MJO's contribution to individual weather episodes.

2. Review of previous work

Previous work on this topic has concentrated mainly on the MJO's impact in tropical northern Australia during (austral) summer. The signal of the MJO in satellite-observed outgoing longwave radiation (OLR), which is a proxy for deep tropical convection, has long been known to extend into northern Australia during summer (e.g., Weickmann et al. 1985; Lau and Chan 1985). As the convectively active phase of the MJO traverses eastward from the Indian Ocean, enhanced convection typically spreads southward into northern Australia and then retreats as the suppressed phase moves in from the west. Composites of multiple events have shown the modulation of rainfall in the far north to be about 5 mm day^{-1} (Hendon and Liebmann 1990; Stringer 1992). More recently, Wheeler and Hendon (2004) showed a greater than threefold increase in the probability of extreme (highest quintile) weekly rainfall in northern Australia during the convectively active MJO phase compared to the suppressed phase. Wheeler and McBride (2005) emphasized the interannual variation of the MJO's impact on northern Australian summer rainfall; in some years its impact is easily recognized in raw rainfall time series, but in others it can barely be discerned.

Comparatively little work has been done on the MJO's impact on Australian rainfall outside of the tropics or in seasons outside summer. The far-field response is not expected to be as pronounced as the direct impact in the tropics because the remote response to the MJO depends upon teleconnections such as the excitation of Rossby wave trains, and their propagation through an ever-changing background flow (e.g., Jin and Hoskins 1995). Nevertheless, a far-field impact on Australian circulation exists. For example, Knutson and Weickmann (1987) found evidence for an association between winds across southern Australia and the MJO in the extended winter season (May–October). These wind anomalies, in fact, are one of the most prominent extratropical circulation features associated with the

MJO anywhere on the globe. This remote impact on winds may lead to a change in weather regime, and thus an indirect rainfall impact.

Some evidence also exists for a far-field response in summer. Knutson and Weickmann (1987) found an extratropical signal in OLR over southern Australia leading the main eastward-propagating convective anomaly in the tropics by approximately a week. This extratropical signal in OLR has appeared in other studies as well (e.g., Hendon and Liebmann 1990). Wheeler and McBride (2005) showed that it was associated with rainfall and occurred in conjunction with anomalous northerly winds across central Australia. It is this extratropical rainfall signal that was presumably extracted by Stone and McKeon (1993) in a study of crop-planting opportunities in eastern inland Australia. Information on whether this rainfall signal extends as far as the southern Australian coast, or whether it also occurs in the equinoctial seasons, however, is lacking.

Finally, there has been one recent published study that has provided some information on the MJO's impact on Australian rainfall outside of the summer season. Donald et al. (2006) computed the maximum difference between the conditional and unconditional cumulative distribution functions (CDFs) for four phases of the MJO during two extended seasons, May–October and November–April. Differences of greater than 5% were found at numerous stations across the country in both seasons.

Motivated by these previous results, we delve further into the impact of the MJO on Australian rainfall. Specifically, we will address the following questions: (i) Is there evidence of an Australia-wide impact of the MJO on rainfall? (ii) How does the impact vary with season? (iii) How does the impact vary using different rainfall metrics (e.g., for the mean compared with defined event probabilities)? And (iv), how are the rainfall changes related to changes in the tropospheric circulation?

3. Data

We use multiple datasets with daily resolution to depict rainfall and circulation, and to define the state of the MJO. The period of analysis is constrained by the availability of satellite OLR data, which were used to construct our MJO index. OLR data are available from June 1974 onward, but with missing data during 17 March 1978 to 31 December 1978. All other datasets are available continuously throughout this period, and we end our analysis in February 2006.

a. Rainfall

We obtained gridded analyses of daily Australian rainfall from the National Climate Centre of the Australian

Bureau of Meteorology. The analyses are derived from daily gauge reports, using a network of approximately 6000 stations spread across the continent and nearby islands. Conversion to a grid is made by the application of a three-pass Barnes successive-correction analysis, with a correlation length scale of 80 km for the outer pass (Mills et al. 1997). The Barnes analysis is performed on a regular 0.25° grid, although the data used in this study are area averaged onto a 1° grid. This averaging aims to provide accurate estimates of daily rainfall averaged over an area rather than accurate estimates of point values. Although technically there are no missing data, we masked out an area in the continental interior that contains few real observations.

b. NCEP–NCAR reanalysis winds and geopotential heights

Global analyses of winds and geopotential heights are obtained from the National Centers for Environmental Prediction–National Center for Atmospheric Research (NCEP–NCAR) reanalysis (Kalnay et al. 1996; Kistler et al. 2001) on a 2.5° grid. Using only data from June 1974, we maximize the benefits of the input of satellite observations into the reanalysis. We are thus confident in the representation of the circulation that it provides.

c. Satellite-observed OLR

OLR data from the National Oceanic and Atmospheric Administration (NOAA) polar-orbiting satellites are used as an input to our MJO index and also as a proxy for deep tropical convection. Interpolation is applied separately to the “day” and “night” maps to remove missing data, and these maps are then averaged to provide a single daily map on a 2.5° grid (Liebmann and Smith 1996).

d. MJO index

The state of the MJO (amplitude and phase) is defined using the Real-time Multivariate MJO index (RMM, available online at <http://www.bom.gov.au/bmrc/clfor/cfstaff/matw/maproom/RMM/>) of Wheeler and Hendon (2004). This index defines the MJO through projection of daily anomaly data onto the leading pair of empirical orthogonal functions (EOFs) of the combined fields of equatorially averaged (15°N – 15°S) OLR, 850-hPa zonal wind, and 200-hPa zonal wind. Longer-time-scale variability resulting from El Niño–Southern Oscillation (ENSO) and other interannual variations with periods longer than about 200 days is removed prior to this projection, but otherwise no temporal filtering is applied.

The RMM index views the MJO in a way that is reminiscent of the original schematic of Madden and

Julian (1972), comprising convectively coupled, vertically oriented, circulation cells that propagate eastward around the globe along the equator. The same equatorially averaged EOFs are applicable in all seasons, thereby providing a consistent measure of the MJO through the seasonal cycle. When viewed in the two-dimensional phase space defined by the two principal component time series (called RMM1 and RMM2; Fig. 2), strong MJO events appear as large anticlockwise excursions about the origin, and weak MJO variability usually appears as a somewhat random movement near the origin. This phase space is used to define eight “strong” MJO phases (labeled 1–8 in Fig. 2), and a “weak MJO” category defined when the amplitude ($\sqrt{\text{RMM1}^2 + \text{RMM2}^2}$) is less than 1. Phases 1 and 2 mark the time when the MJO’s convective envelope is centered near the western Indian Ocean, and phases 7 and 8 mark the time when it is near the date line in the Pacific.

Despite using no intraseasonal time filtering, the index strongly discriminates to the 30–80-day MJO signal. Consequently, RMM1 and RMM2 are highly predictable when using themselves as predictors at an initial time. For example, Maharaj and Wheeler (2005) obtained a forecast correlation skill of ~ 0.6 with a vector autoregressive model at a 12-day lag.

4. Methods

Composites of rainfall and circulation are computed for each of the eight phases of the MJO plus the weak MJO category, and separately during each 3-month season [December–February (DJF), March–May (MAM), June–August (JJA), and September–November (SON)]. Composites are formed by assigning every day of the historical record into one of the nine categories. For example, the time series of MJO categories [$\text{MC}(t)$] from 1 to 22 December 2003 (as can be deduced from Fig. 2) is

$$\text{MC}(t) = (0, 0, 2, 2, 2, 2, 3, 3, 3, 3, 3, 3, 3, 4, 4, 4, 5, 5, 5, 5, 5),$$

where “0” represents the weak MJO category, and the other numbers refer to the MJO phase whenever the amplitude of the MJO > 1 . For this particular episode, the MJO develops (attains amplitude greater than 1) when the convective envelope is located over the Indian Ocean (phase 2 in Fig. 2), but in general each new MJO event or sequence of events may start from almost any location (Matthews 2008).

For composites of mean daily anomalies, we first form anomalies by subtracting their multiyear climatological

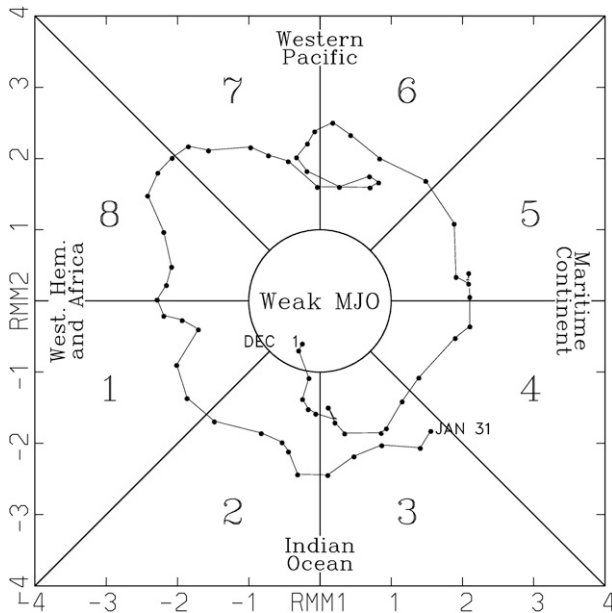


FIG. 2. Phase-space representation of the two-component MJO index, for the period 1 Dec 2003–31 Jan 2004. Each dot represents the value of the index on a particular day, with the starting and ending days labeled. Also shown are the eight defined phases of the MJO and the region used to signify weak MJO activity. Also labeled (with words) are the approximate locations of the near-equatorial enhanced convective signal of the MJO for each quadrant of the phase space (e.g., the “Indian Ocean” for phases 2 and 3).

means for each season. For example, for an arbitrary gridded field $F(x, y, t)$ anomalies are expressed as $F'(x, y, t) = F(x, y, t) - \bar{F}(x, y, s)$, where s refers to the season (DJF, MAM, JJA, or SON) and the overbar is the mean for that season. While a constant climatology over each 3-month season ignores the smoothly varying nature of the seasonal cycle, this is of little or no consequence because the MJO shows no obvious phase locking to the calendar date. Composites indicated as “daily anomalies” are therefore an average of the anomaly field data $F'(x, y, t)$ over the contemporaneous (i.e., with zero lag) days that fall in each MJO category for that particular season. All the composites of wind, geopotential height, and OLR data we show are formed in this way.

For our analysis period, the composites for each phase of the MJO contain about 200 days and the weak MJO category contains about 1000 days. Noting that the average period of the MJO is ~ 50 days, it takes an average of 6 days for the MJO to progress through each of the eight phases. Hence, each phase composite is based on approximately 33 unique MJO events (i.e., $\approx 200/6$).

We also generate “probability composites” for rainfall. We do this with total rainfall data $R(x, y, t)$ by counting the number of days at each grid location for

each composite phase for which R is greater than a predefined rainfall threshold T , and then dividing by the total number of days in that composite phase to form a probability. We do this using daily and 7-day running mean (overlapping weekly) rainfall. For the overlapping weekly data, we form composites using the MJO category occurring on the middle day, providing the best estimate of the contemporaneous relationship. The threshold T can be a function of space and season, or constant depending on the purpose for which the information is to be used. Here we show results using T set to (i) the upper tercile (i.e., the 67th percentile) or highest decile (i.e., the 90th percentile) of weekly rainfall at each grid location (for which T is a function of x , y , and s), and (ii) 1 mm day^{-1} everywhere. The latter can be used to infer the probability of a *rain day* better than using a 0-mm threshold because even a trace amount of rain at a single station within a grid square will give a greater than zero average for the 1° square.

Statistical significance for the rainfall composites is judged using a nonparametric resampling approach whereby we successively shift the time sequence of the observed MJO phases $MC(t)$ relative to the time series of rainfall and recompute the composite anomalies and probabilities. This time shifting and recalculation is done an arbitrary 400 times, thereby producing 400 synthetic realizations of the composite values (the *null distribution*) with which to compare the actual contemporaneous composite (the *observed test statistic*; see Wilks 2006). We do this shifting in even steps, using data only from the desired season. For example, for the DJF season we string together the MJO category and rainfall data from different years (i.e., joining each December with the previous February) and loop the end of the series in February 2006 back to the beginning in December 1974. Then, with a total of 2857 days in both time series for DJF (noting some missing data in 1978), we apply evenly spaced shifts that vary between 50 and $2857 - 50$ days (spaced 6 or 7 days apart for 400 samples), recomputing the composites at each grid point. Knowing that the MJO is not perfectly periodic and that the MJO decorrelates in less than 50 days (Salby and Hendon 1994), this time shifting and recalculation of the composites provides an accurate estimate of what can be obtained by chance alone. The 400 synthetic realizations of the composites are then sorted from lowest to highest, and we take the 10th (2nd) highest and 10th (2nd) lowest as the thresholds for significance at the 5% (1%) level for a two-sided test. The advantage of this resampling approach is that it maintains the autocorrelation (redness) of the MJO index and rainfall data, makes no assumptions about the normality of the data, and can be applied fairly to the different test statistics

(i.e., the anomaly versus probability composites). Furthermore, it automatically takes into account the different number of days in each MJO phase. The thresholds for significance were insensitive to varying the number of synthetic realizations between 200 and 400, so using 400 realizations was deemed to be enough.

For the global wind and geopotential height anomaly composites, on the other hand, statistical significance is judged using a computationally inexpensive parametric test. Under the assumption that the field data (F') are normally distributed, the composites are judged to be significantly different from zero at the 20% (10%) [5%] level using a local t test if

$$t = \frac{\left| \sum_{\text{MC}} F'/N \right|}{\sigma \sqrt{1/N_{\text{eff}}}} > 1.3 \text{ (1.67) [2.0]}.$$

Here $\sum_{\text{MC}} F'/N$ is the anomaly field composite for the MJO category (MC) of interest, σ is the daily standard deviation of F' (the field) computed over the season, N_{eff} is the effective sample size approximated by

$$N_{\text{eff}} \cong N \frac{1-\rho}{1+\rho}$$

(e.g., Wilks 2006), N is the number of days in the category, and ρ is the lag 1 autocorrelation coefficient of F' over the season. In DJF, typical values of ρ over the domain of interest are 0.8 for 500-hPa geopotential height data, 0.7 for 500-hPa zonal wind, and 0.5 for 500-hPa meridional wind, resulting in a greatly reduced N_{eff} . All significance tests are computed and applied independently at each grid location. Limited comparisons of this method with the resampling approach for significance show that it results in a relatively consistent estimate (see also Hendon et al. 2007).

Noting that the choice of significance level is arbitrary, we mostly display anomalies or probabilities irrespective of significance, and use shading or symbols to delineate those values that reach the conventional thresholds for significance.

5. Results

a. Weekly rainfall probabilities (upper tercile) and 850-hPa winds

We begin by showing composites of 850-hPa wind anomalies and probabilities of weekly rainfall occurring in the upper tercile for each of the eight MJO phases (Figs. 3–6). We display the anomalous winds as vectors, and contour rainfall probabilities scaled by the local mean probability of rainfall exceeding the computed

threshold. This local mean probability is nominally 33% except in seasonally very dry regions (e.g., northern Australia in JJA) where the upper tercile threshold drops to 0 mm week⁻¹ and the probability of getting any rainfall in a week is less than 33%. In those regions we set the threshold at 0 mm and scale by the slightly reduced mean probability. The actual rainfall thresholds used are displayed in the bottom-right panel of each figure. Probability ratios greater (less) than 1.0 indicate an enhanced (reduced) probability of rainfall exceeding the threshold. Additionally shown in each of Figs. 3–6 are the respective climatological mean rainfall and 850-hPa vector wind (middle-right panels).

Comparison of Figs. 3–6 shows that the greatest swings in rainfall probability occur during summer (DJF; Fig. 3) with ratios in excess of 1.6 occurring across large areas of northern Australia in phases 5 and 6, and ratios less than 0.6 in phases 1 and 2. That is, the conditional probability of receiving a week's accumulation of rainfall in the climatological upper tercile shifts from being less than 20% ($0.6 \times 33\%$) in phases 1 and 2, to greater than 53% ($1.6 \times 33\%$) in phases 5 and 6. This enhanced likelihood of rainfall during phases 5 and 6 occurs in conjunction with anomalous 850-hPa westerlies across the far north of the domain, maximizing at about 5 m s⁻¹ in phase 6. Similarly, suppressed rainfall in phases 1 and 2 occurs in conjunction with anomalous easterlies. In both cases, the winds slightly lag the rainfall, consistent with previous studies (e.g., Hendon and Liebmann 1990).

Also evident in Fig. 3 is an extratropical rainfall signal over central and southern Australia, which leads the tropical signal by one or two phases; phases 3 and 4 have enhanced probabilities of being wet in the extratropics, whereas phases 5 and 6 are wet in the tropics. The enhanced extratropical rainfall of phases 3 and 4 occurs in conjunction with predominantly northerly wind anomalies. This combined wind–rain signal was highlighted by Wheeler and McBride (2005), but the extension to the southern coast was not previously appreciated. The northerly anomalies during phases 3 and 4 across southern Australian correspond to actual northerlies, because the mean winds (middle-right panel) have a near-zero meridional component. Conversely, reduced rainfall probabilities occur in central and southern Australia in phases 8 and 1, albeit associated with comparatively weaker southerlies. The weak MJO category (top-right panel), by comparison, shows weak rainfall signals and wind anomalies, as is the case for all other seasons (see also Figs. 4–6).

For autumn (MAM; Fig. 4), the patterns of composite rainfall are not appreciably different to those in summer (Fig. 3) except that the signals are generally weaker in the

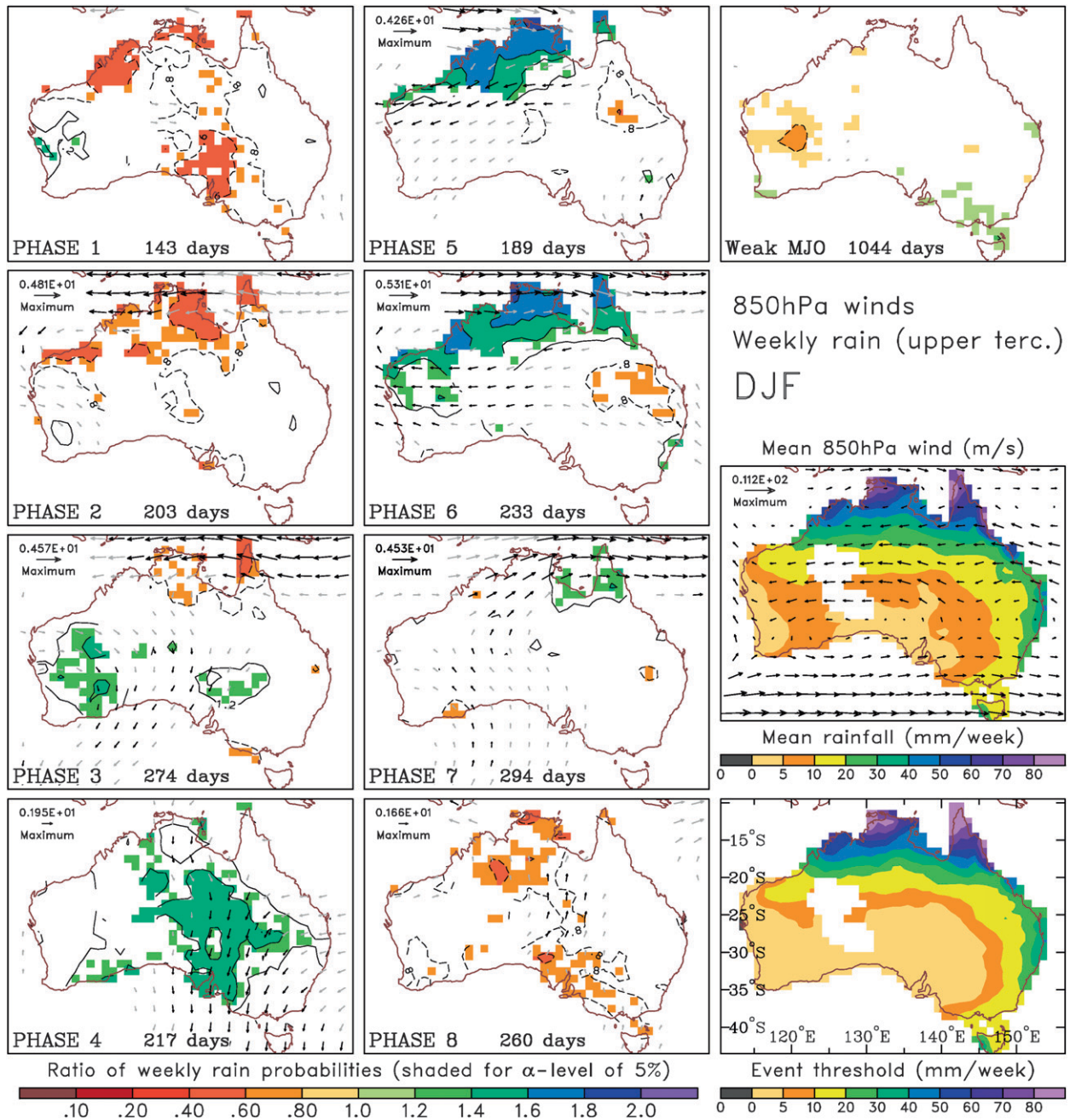


FIG. 3. (left and middle) MJO composites of weekly rainfall probabilities (contours and shading) and 850-hPa wind anomalies (vectors) for the summer (DJF) season for phases 1–8. Rainfall probabilities refer to the chance of weekly rainfall exceeding the upper tercile, expressed as a ratio with the mean probability (nominally 33%). Contour levels are provided in the key with contours <1.0 dashed and the 1.0 contour omitted. Shading varies with each contour, but is only provided where the signal is determined to be locally significant at the 5% level. For the winds, black vectors are determined to be significant at the 5% level, and gray vectors at the 20% level, with the magnitude of the maximum vector in each panel provided. (top right) As above, except for the weak MJO category. (middle right) Climatological DJF mean winds (vectors) and mean rainfall (shading). The vector length in the mean plot is scaled to be exactly half that of the vectors in the MJO composite plots. (bottom right) Threshold for an upper tercile weekly rainfall event.

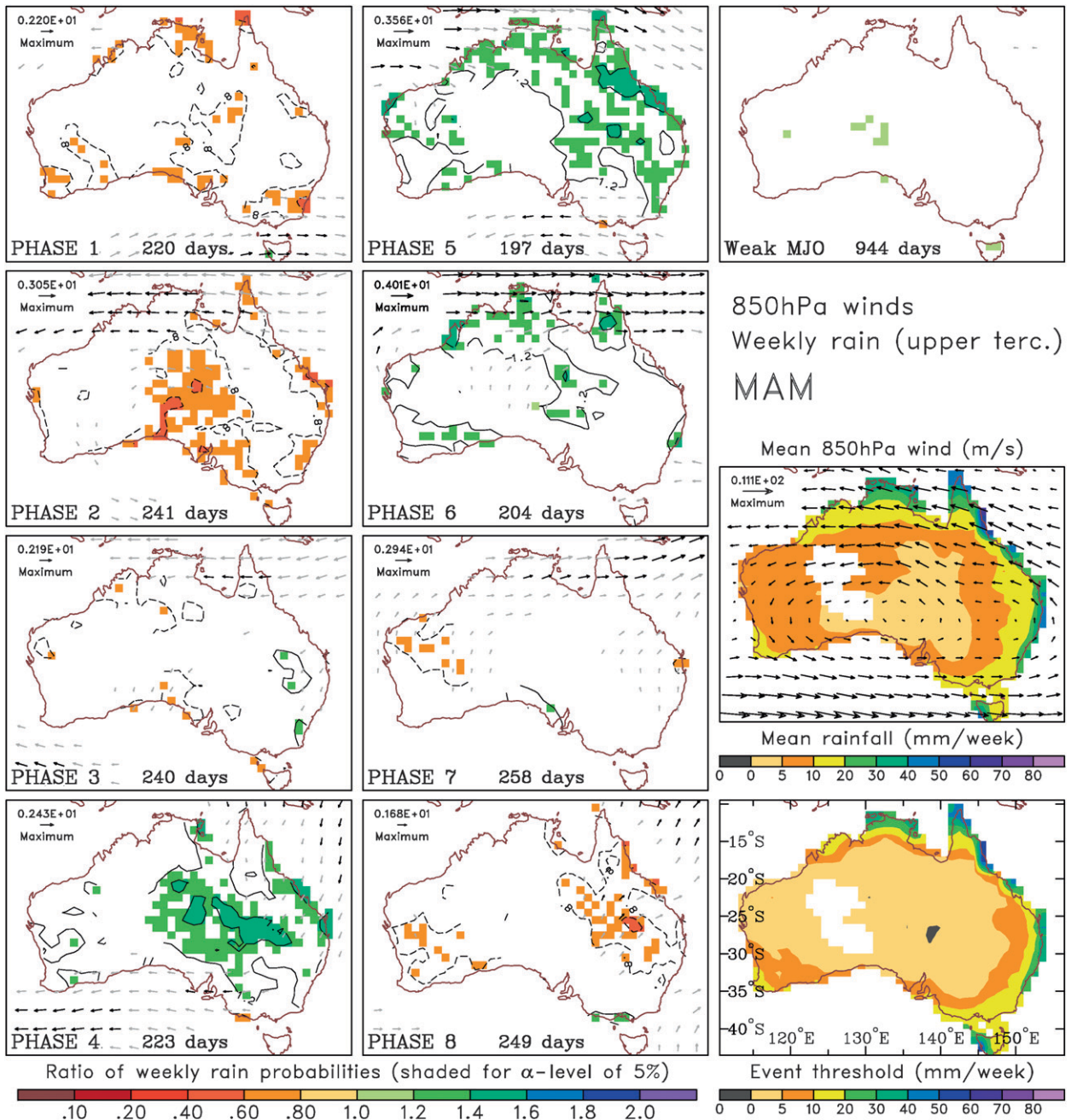


FIG. 4. As in Fig. 3, but for the autumn (MAM).

far north. This is despite some rather large differences in the climatological mean rainfall and winds. One appreciable difference, however, is central-south Queensland for phases 5 and 6; in summer this region experiences reduced probabilities of being wetter than the upper tercile threshold, but in autumn it experiences increased probabilities, which coincide with weak low-level cyclonic wind anomalies (not shown).

In contrast, the composite rainfall signals are much different in winter (JJA; Fig. 5) compared with summer or autumn. Although the tropical low-level wind anomalies remain much the same (e.g., westerlies in phases 5 to 7 and easterlies in phases 1 to 3), the regions of suppressed and enhanced tropical rainfall must now be understood in terms of the local strengthening or weakening of the trade winds and associated orographic

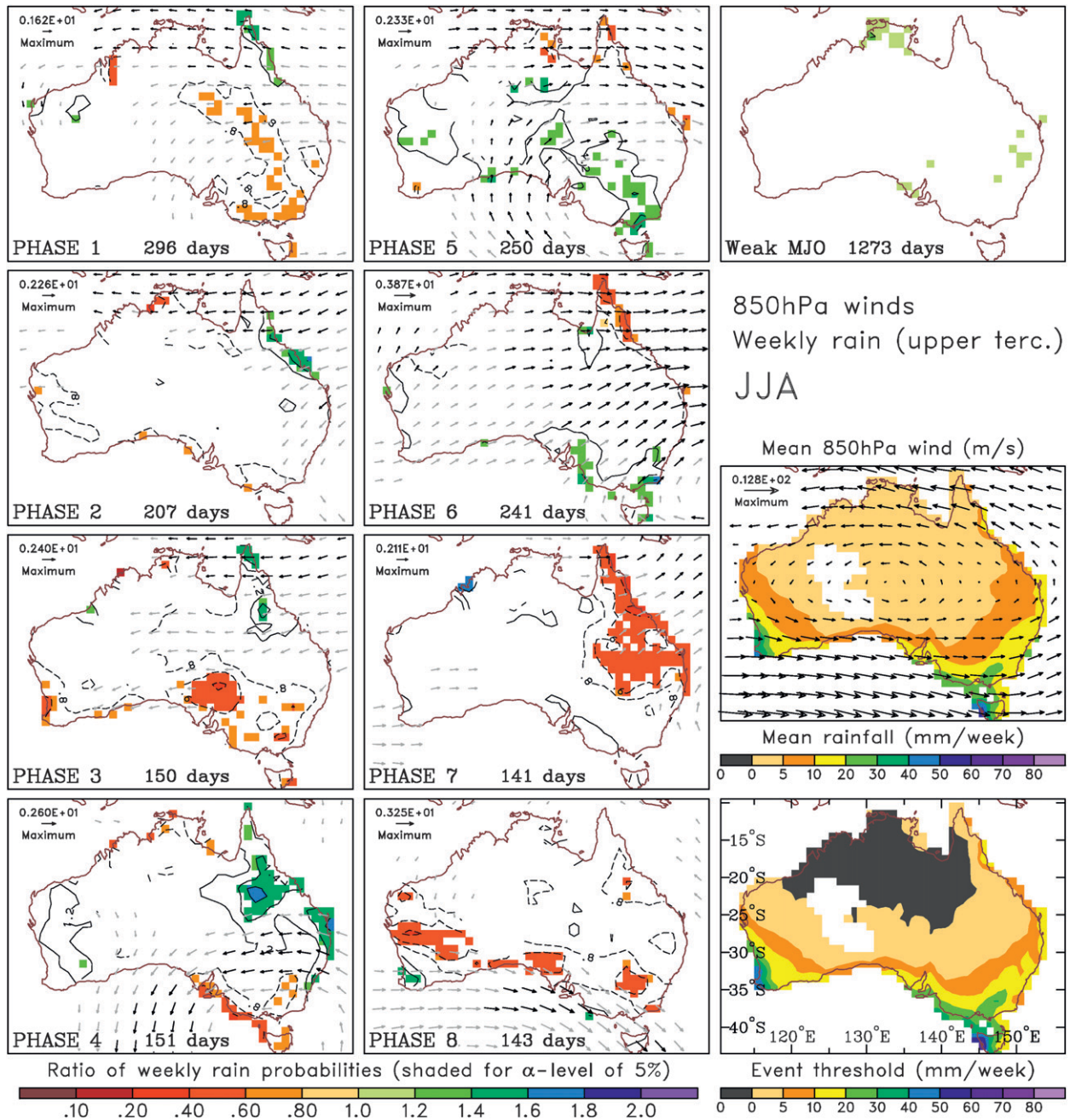


FIG. 5. As in Fig. 3, but for the winter (JJA).

effects along the east coast, rather than resulting from the direct tropical convective signal of the MJO. For example, rainfall along the northeast coast (northeast Queensland) is suppressed when the trades are weakened by westerly anomalies during phases 5, 6, and 7, and enhanced when the trades are strengthened during phases 1, 2, and 3. Phase 4 also shows enhanced rainfall along the east coast, but extending farther to the south,

occurring as the enhanced trade wind flow in the north eases, but with the development of easterly anomalies along central to southern parts of the coast.

In southern Australia, however, the situation in winter appears somewhat more complicated. First, the linearity between opposite MJO phases (e.g., phases 4 and 8 in Fig. 5) is reduced for both the rainfall and winds. Second, there often appears a rapid transition from one

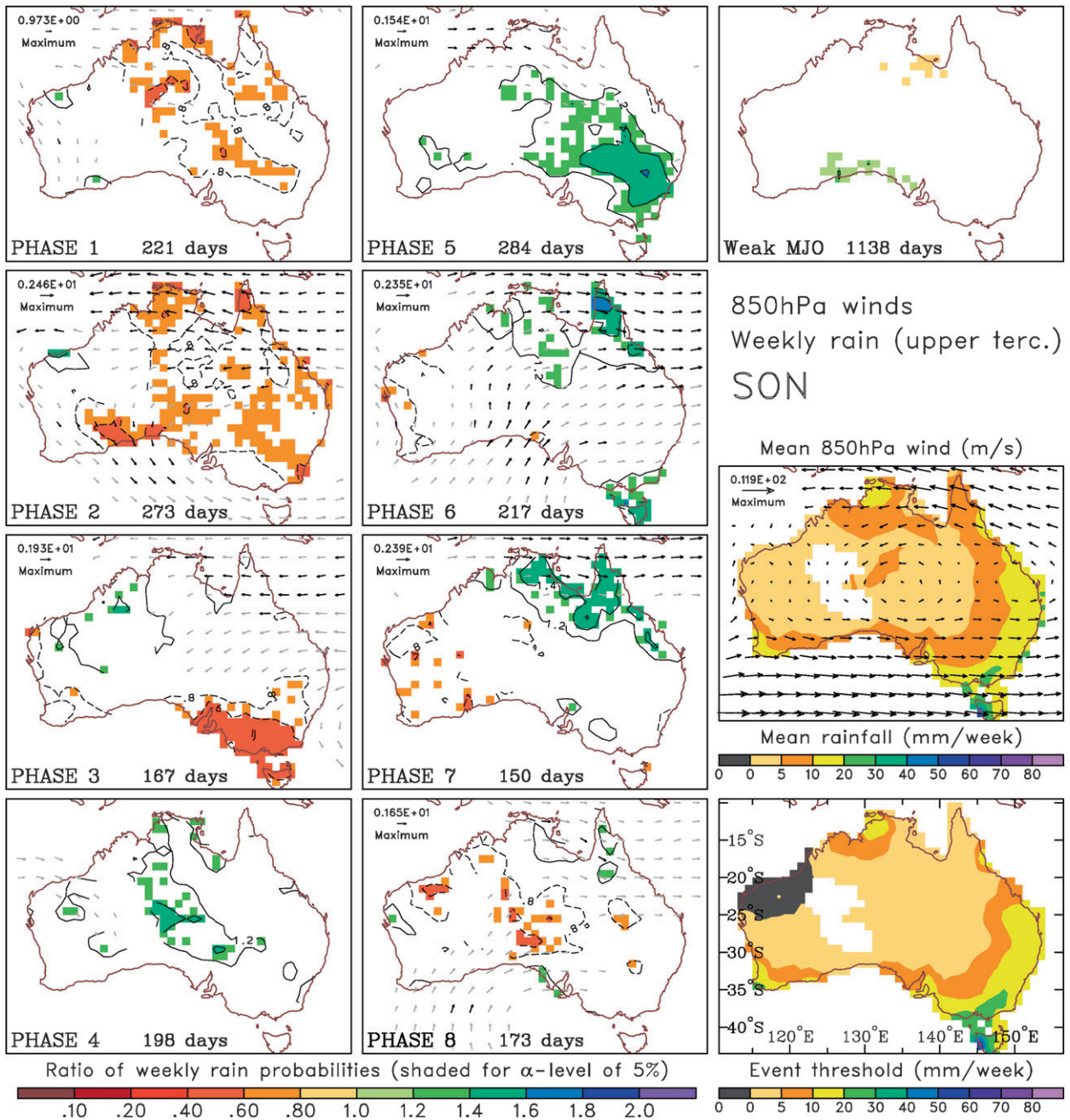


FIG. 6. As in Fig. 3, but for the spring (SON).

phase to the next. For example, along the coast of southeastern Australia from about Adelaide (35°S, 139°E) to Wilsons Promontory (39°S, 147°E), the rainfall signal switches from being dry in phases 3 and 4 to wet in phases 5 and 6. Although these probability swings are weak, they are statistically significant (at the 5% level), and occur in conjunction with a near reversal in the 850-hPa level wind anomalies. Even such small rainfall sig-

nals are potentially of great economic importance given that rainfall in the JJA period is critical for yield formation of agricultural crops grown in the region. We further discuss these signals in section 6.

Lastly, in spring (SON; Fig. 6) the rainfall composite signals become, for the most part, like those for summer and autumn, with primarily enhanced rainfall probabilities across Australia in phases 5 and 6, and reduced

probabilities in phases 1 and 2. Notable, however, is the concentration of the phase 5 wet signal to the south-eastern quadrant of the country unlike that for summer and autumn, and the dry signal in the far southeast corner in phase 3, which resembles more closely that for winter. We will show in section 6 that the suppressed rainfall signal in phase 3 occurs in conjunction with a strong anticyclonic anomaly in the midlevel circulation.

b. Comparison of different rainfall metrics

The previous section described the impact of the MJO on rainfall only in terms of the conditional probability of weekly rainfall exceeding the upper tercile. We now explore how these results extend to other rainfall metrics. For example, does daily mean rainfall and/or the number of rain days go up and down consistently in the same regions and phases? This question is of scientific as well as of practical importance: the choice of the metric will determine the relevance of the information for decision making. We examine this question for three representative regions in Fig. 7 for which we show the variation of (i) the probability of weekly rainfall in the upper tercile (as before), (ii) the probability of weekly rainfall in the highest decile, (iii) the probability of the daily rainfall exceeding 1 mm, and (iv) the mean daily rainfall anomaly. The mean daily anomaly is typically computed in meteorological studies with no regard to applications. The weekly decile metric is relevant to applications such as soil waterlogging, and the daily 1-mm threshold is useful for applications requiring no rain in a day such as for the spraying of herbicides. Each metric is computed on the 1° grid then area averaged over the regions shown, and statistical significance is indicated where at least half the grid squares in each region are individually 5% or 1% significant (by our resampling method). These three regions represent a climatologically diverse selection, each of which is significant for the agricultural and economic productivity of Australia.

Of primary interest in Fig. 7 is the extent to which the different rainfall metrics show signals in the same direction. For the most part, they do, although with some notable exceptions. One exception is in the southern Queensland box in DJF (Fig. 7c); the daily anomaly (black curve) shows a pronounced maximum in phase 8, but the weekly upper tercile probability (blue curve) has its maximum in phase 4. Similarly in this region in MAM, the daily anomaly signal peaks in phase 6, but all probability metrics peak in phase 4. Indeed, in many of the graphs the daily anomaly curves have a tendency to be noisier than the probability metrics, with a greater tendency to jump up and down from one phase to the next (e.g., DJF in southern Australia and DJF and

MAM in southern Queensland). This is a consequence of outlier rainfall events; an outlier event (e.g., rain exceeding 100 mm in a day) will influence the daily anomaly to a much greater extent than the probability of exceeding a specified threshold. Thus, it appears that the peak in the daily anomaly in the southern Queensland box in DJF phase 8 has occurred by chance, without being indicative of a robust MJO signal.

Also of interest in Fig. 7 is the total number of phases for which we compute a significant signal when summed over all seasons and regions. The total is 15 for the weekly upper tercile probability, 9 for the probability of daily rainfall >1 mm, 8 for the daily anomaly, and 6 for the weekly highest decile probability. Examination of the full set of maps for each metric (not shown) confirms this tendency for the weekly tercile metric to gain overall greatest statistical significance. The explanation is derived from (i) the tercile metric is less influenced by outlier events than the daily anomaly (as discussed above); (ii) upper-tercile events occur more often than highest decile events, providing a greater number of cases for which to gain statistical confidence; and (iii) the weekly tercile threshold is a relative measure that varies with location and season, providing greater flexibility and relevance than the constant 1-mm threshold.

6. Dynamical associations and explanations

Greater confidence and understanding of the rainfall signals described in section 5 can be gained by examining the large-scale circulation anomalies that occur in conjunction with them, especially for those rainfall signals occurring away from the MJO's tropical convective anomaly. Previous work has established that some of the extratropical circulation anomalies associated with the MJO are explained as diabatically forced Rossby wave trains modified by the background mean flow and by feedbacks from high-frequency synoptic eddies (e.g., Ferranti et al. 1990; Matthews and Kiladis 1999; Matthews et al. 2004). The extratropical circulation response to diabatic heating associated with tropical convection is dependent not only on the background mean flow, but on the magnitude, positioning, and time evolution of the diabatic (convective) forcing (e.g., Ting and Sardeshmukh 1993; Jin and Hoskins 1995; Bladé and Hartmann 1995). In this study, we concentrate not on these mechanisms per se, because the existence of these tropical-extratropical teleconnections has already been established. Rather, we focus on further explanation and quantification of the composite rainfall signals.

Composites of large-scale circulation anomalies for phases 2, 3, 4, and 5 at the 500-hPa level are shown in Figs. 8–11 for each season. These phases represent an

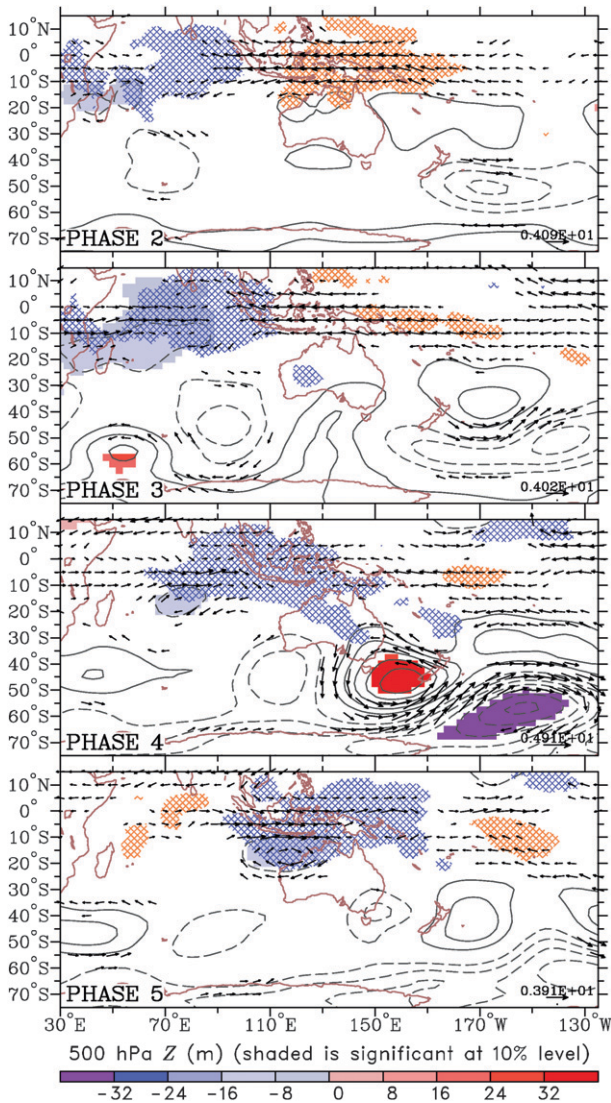


FIG. 8. Summer (DJF) composite OLR (cross-hatching), 500-hPa wind (vectors), and 500-hPa geopotential height (contours and shading) anomalies for MJO phases 2, 3, 4, and 5. Blue cross-hatching indicates OLR anomalies $< -10 \text{ W m}^{-2}$, and orange cross-hatching for anomalies $> +10 \text{ W m}^{-2}$. Vectors are plotted only where they are determined to be locally significant at the 10% level. The contour interval for geopotential height is 8 m, with the zero contour omitted and negative contours dashed. Blue-red shading is used only where the geopotential height anomalies are determined to be significant at the 10% level. The size of the maximum vector is listed at the bottom right.

a. Summer (DJF)

In summer (Fig. 8), enhanced tropical convection, as indicated by negative OLR anomalies, shifts from the Indian Ocean in phase 2 to the Australian–Indonesian monsoon region by phase 5. In the Indian Ocean, the OLR anomaly is bounded between about 12°N and 20°S , which is as far south as it extends for any season

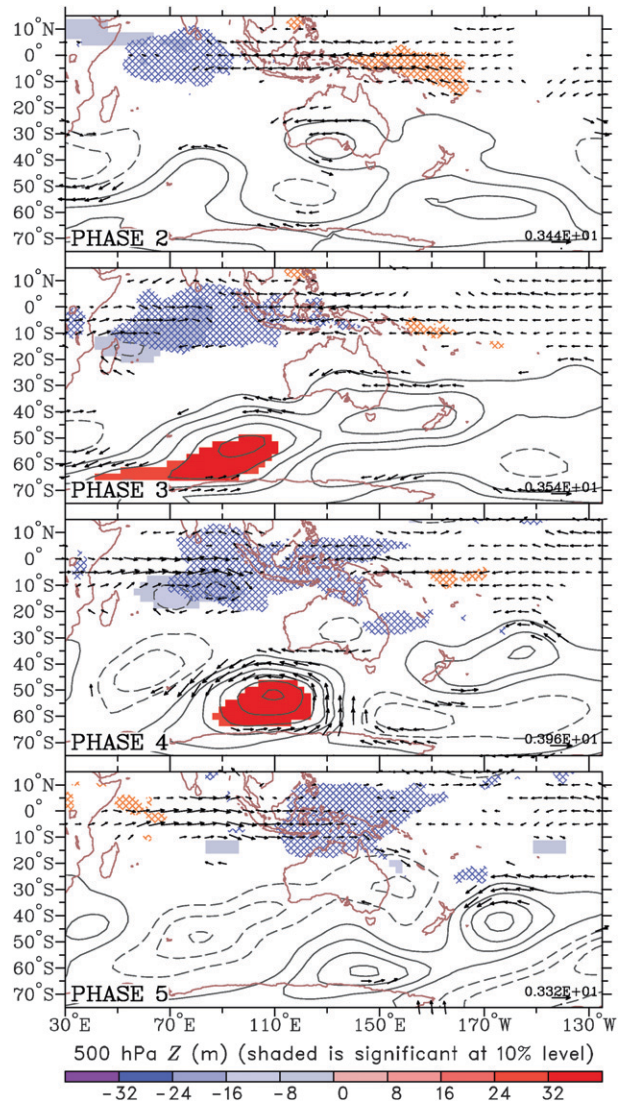


FIG. 9. As in Fig. 8, but for the autumn (MAM).

(cf. Figs. 9–11). Over Australia, however, a negative OLR anomaly appears at extratropical latitudes in phases 3 and 4, preceding the main tropical convective signal in phase 5. This is the same signal highlighted in the rainfall in the previous section (e.g., Fig. 3). Thus, the enhanced rainfall in the extratropics occurs in conjunction with increased high-level clouds, which in phase 4 are linked continuously back to the tropics as a relatively narrow band oriented toward the northwest. This OLR signature bears a close resemblance to what is commonly known as a northwest Australian cloud band. Northwest cloud bands may occur in any season, each event typically lasting over several days, although they have been shown to be more frequent in winter (Tapp and Barrell 1984).

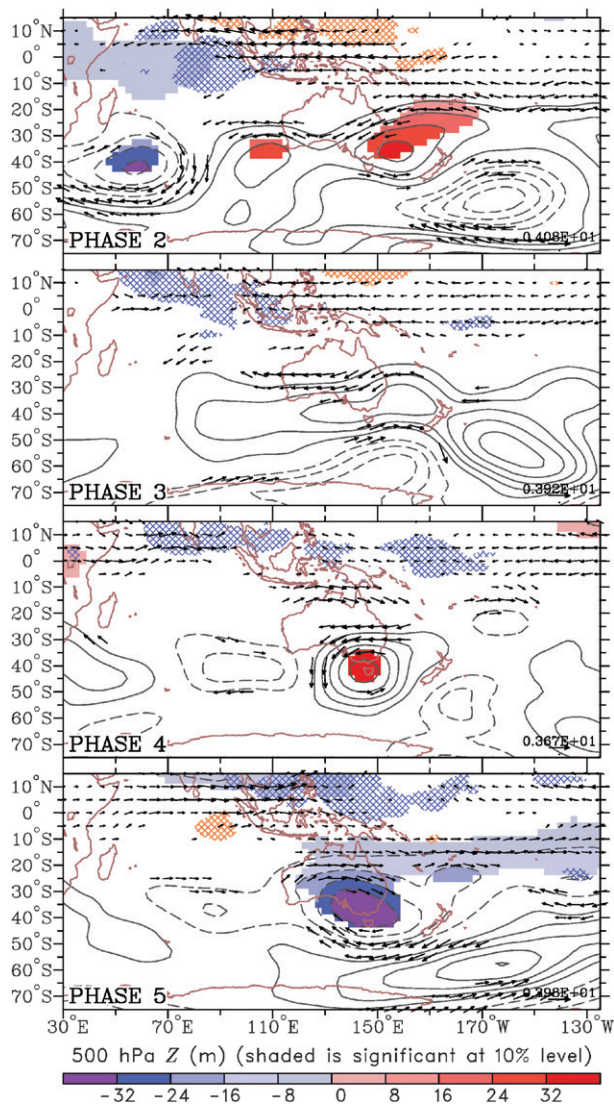


FIG. 10. As in Fig. 8, but for the winter (JJA).

The anomalous winds at the 850-hPa level in association with the extratropical rainfall signal in phases 3 and 4 are predominantly northerly (Fig. 3). At the 500-hPa level, these northerlies are associated with a mid-latitude wave train (Fig. 8); in phase 2 a weak negative geopotential height anomaly exists over the southwest Indian Ocean that subsequently shifts eastward, strengthens, and undergoes downstream development. Then, by phase 4 a positive height anomaly develops over the Tasman Sea, consistent with, and reinforcing, the lower-tropospheric northerlies highlighted in Fig. 3. These low-level northerlies suggest a possible role for moisture transport from the tropics for the enhanced extratropical rainfall. Also, a slow-moving “blocking high” to the south and east of Australia is characteristic

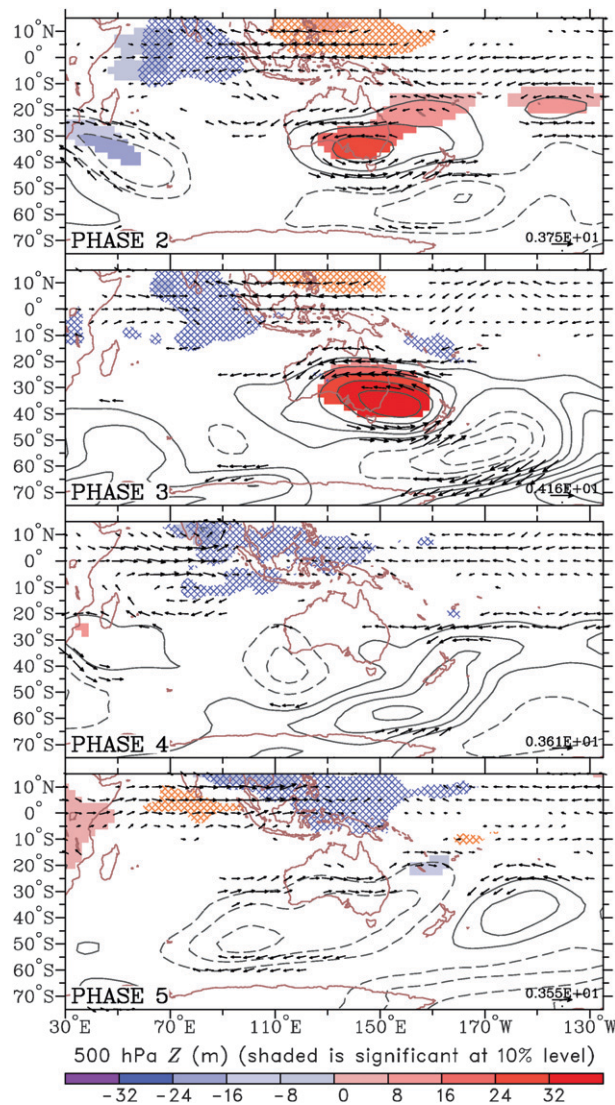


FIG. 11. As in Fig. 8, but for the spring (SON).

of many summer (and early autumn) synoptic weather events producing widespread high rainfall in southern Australia (e.g., Zhao and Mills 1991).

b. Autumn (MAM)

Although the tropical circulation anomalies in autumn (Fig. 9) closely resemble those in summer (Fig. 8), the extratropical anomalies show some noticeable differences. Similar to summer, in phases 2 and 3 weak anomalously high geopotential heights exist over southern Australia and to its east in the Tasman Sea. In phase 4, however, the anomalous 500-hPa high that existed over the Tasman Sea in summer is now split to the west and east. The only statistically significant (at the $\sim 10\%$ level) extratropical height anomaly during these phases

in autumn is the high that exists to the south and west of Australia in phases 3 and 4. Thus, unlike summer, there are no significant low-level northerly anomalies across the center of the continent in phases 3 and 4. Consistent with the lack of northerly anomalies, there are comparatively weaker (although still statistically significant in phase 4) extratropical rainfall signals in these phases in autumn (Fig. 4). Compared with summer, enhanced rainfall and coincident negative anomalous OLR (Fig. 9) are focused farther east and north in phase 4. Like in summer, however, this OLR anomaly is placed between a high to its east and a low to its west indicative of northerly anomalies along the northeast coast and to eastern parts of Australia (Fig. 4).

c. Winter (JJA)

One of the more striking winter rainfall signals associated with the MJO is the relatively quick transition from dry conditions in southern Australia in phases 3 and 4 to wet conditions in phases 5 and 6 (Fig. 5). The circulation anomalies at the 500-hPa level (Fig. 10) show an almost stationary high geopotential height anomaly over southeastern Australia during phases 2–4, and associated easterly anomalies at mid- and low levels over eastern and southern Australia (Figs. 5 and 10). This situation rapidly changes, however, between phases 4 and 5, as low height anomalies move into the region from both the north and west and become established over southeastern Australia in phase 5. The enhanced (suppressed) rainfall in southern Australia in winter is thus more closely aligned with the center of a large-scale area of low (high) geopotential height, rather than with anomalous northerly (southerly) winds as occurs in autumn or summer.

d. Spring (SON)

Finally, we are interested in the origin of the reduced springtime rainfall in the southeast during phase 3 (Fig. 6). The springtime 500-hPa extratropical circulation anomalies (Fig. 11) resemble those occurring in winter (Fig. 10), although there are also some similarities with those in summer (Fig. 8). Such similarities between atmospheric anomalies across different seasons, being computed from completely independent data, help increase our confidence in the reproducibility of the results. Compared to winter, however, the anomalous high over southern Australia reaches its peak intensity in phase 3 instead of phase 4. Thus the dry signal in spring during phase 3 appears well explained by the implied large-scale subsidence existing within the extratropical high. Contrasting with this, phases 4 and 5 in spring show wet signals extending across a wide range of latitudes and longitudes (Fig. 6), and these appear

best associated with northwesterly anomalies originating from the eastern Indian Ocean (Fig. 6), in a similar fashion to what occurs in summer in phases 3 and 4.

7. Conclusions

We have examined in detail the impact of the MJO on Australian rainfall and circulation, separating the impact into eight different nonweak MJO phases, and the four different seasons. Overall, the greatest rainfall impact occurs in northern Australia in summer, as could be expected, but in every season rainfall impacts are found in most parts of Australia that are associated with circulation anomalies. Using a compositing approach and a number of different rainfall metrics, we find the MJO's impact on rainfall in Australia is mostly linear in summer and autumn with opposite rainfall signals occurring in opposite phases of the MJO. In winter and spring, however, notable nonlinearities exist, especially over southern Australia, thus justifying our approach of compositing for multiple MJO phases. Of the different rainfall metrics we examine, the probability of weekly rainfall in the upper tercile was found to be the most effective for extracting a significant signal. To aid decision making within climate sensitive sectors such as agriculture, our approach can be readily applied to other climatological metrics beyond rainfall (e.g., temperature), and to other regions of the globe. Southeast Asia, in particular, seems to be ideally situated for important MJO impacts that may benefit from a similar approach.

Explanation of the rainfall impacts has been derived from an examination of atmospheric circulation anomalies. In the north of Australia in all seasons except winter, the MJO's impact on rainfall is explained by the direct impact of the MJO's tropical convection anomalies. In winter, however, the MJO's tropical convection shifts north of Australia, and the impact on rainfall in northern Australia is then mostly confined to the northeast where it appears to result from the local modulation of the trade winds as they impinge upon the coast. In extratropical Australia, however, the MJO's impact on rainfall appears best associated with induced vertical motion occurring within remotely forced anomalous extratropical highs and lows and anomalous low-level meridional winds that cause variations in the transport of moisture from the tropics. The former association most applies in far southeastern Australia in winter and spring, whereas the latter most applies in summer and autumn. For the latter, the extratropical rainfall signal is found to lead the main tropical convective signal by about a phase (i.e., several days), for example, from phase 4–5 in summer. During these situations, the circulation and high-level cloud (OLR) anomalies associated with the extratropical

rainfall are also suggestive of northwest cloud bands (e.g., Tapp and Barrell 1984).

In addition to our increased understanding, these results provide a basis for estimating the MJO's contribution to individual weather episodes. Using an index of the MJO that can be computed in real time allows for the examination and estimation of this contribution in real time. Also, as the MJO is arguably the most predictable of all intraseasonal phenomena, the impacts presented are likely among the most predictable on that time scale. The results will thus aid future work on intraseasonal prediction in Australia, whether it is by statistical or dynamical models.

Although these results go a long way toward explaining a portion of the intraseasonal variability in Australian rainfall and circulation, it is important to note that the results presented only indicate the average influence of multiple MJO events; given that no MJO event is the same, the impact of any individual event, if it could be determined, would differ from that shown and may be even larger and, perhaps, more predictable.

Acknowledgments. This research was supported in part by the Managing Climate Variability Program of Land and Water Australia, through the multi-institution collaborative project QPI62. H. M. initiated this project while employed by the Queensland Department of Primary Industries and Fisheries, Australia. The NCEP–NCAR reanalysis were obtained from the Physical Sciences Division of NOAA/ESRL, and we thank NOAA as a whole for their measurement and provision of the OLR data. Thanks to Robert Fawcett for his part in producing the gridded rainfall dataset and to Fiona Lo for her assistance in retrieving it. We also thank James Risbey, Nicolas Fauchereau, Guomin Wang, Graham Mills, Aline de Maia, Benjamin Pohl, Ian Jolliffe, and Adrian Matthews for their comments.

REFERENCES

- Barlow, M., M. Wheeler, B. Lyon, and H. Cullen, 2005: Modulation of daily precipitation over Southwest Asia by the Madden–Julian oscillation. *Mon. Wea. Rev.*, **133**, 3579–3594.
- Bladé, I., and D. L. Hartmann, 1995: The linear and nonlinear extratropical response of the atmosphere to tropical intraseasonal heating. *J. Atmos. Sci.*, **52**, 4448–4471.
- Bond, N. A., and G. A. Vecchi, 2003: The influence of the Madden–Julian oscillation on precipitation in Oregon and Washington. *Wea. Forecasting*, **18**, 600–613.
- Carvalho, L. M., C. Jones, and B. Liebmann, 2004: The South Atlantic convergence zone: Intensity, form, persistence, and relationships with intraseasonal to interannual activity and extreme rainfall. *J. Climate*, **17**, 88–108.
- Donald, A., H. Meinke, B. Power, A. H. N. Maia, M. C. Wheeler, N. White, R. C. Stone, and J. Ribbe, 2006: Near-global impact of the Madden-Julian oscillation on rainfall. *Geophys. Res. Lett.*, **33**, L09704, doi:10.1029/2005GL025155.
- Ferranti, L., T. N. Palmer, F. Molteni, and E. Klinker, 1990: Tropical–extratropical interaction associated with the 30–60 day oscillation and its impact on medium and extended range prediction. *J. Atmos. Sci.*, **47**, 2177–2199.
- Gadgil, S., 2003: The Indian monsoon and its variability. *Annu. Rev. Earth Planet. Sci.*, **31**, 429–467.
- , P. R. Seshagiri Rao, and S. Sridhar, 1999: Modelling impact of climate variability on rainfed groundnut. *Curr. Sci.*, **76**, 557–569.
- Hendon, H. H., and B. Liebmann, 1990: The intraseasonal (30–50 day) oscillation of the Australian summer monsoon. *J. Atmos. Sci.*, **47**, 2909–2924.
- , D. W. J. Thompson, and M. C. Wheeler, 2007: Australian rainfall and surface temperature variations associated with the Southern Hemisphere annular mode. *J. Climate*, **20**, 2452–2467.
- Jin, F., and B. J. Hoskins, 1995: The direct response to tropical heating in a baroclinic atmosphere. *J. Atmos. Sci.*, **52**, 307–319.
- Jones, C., 2000: Occurrence of extreme precipitation events in California and relationships with the Madden–Julian oscillation. *J. Climate*, **13**, 3576–3587.
- Kalnay, E., and Coauthors, 1996: The NCEP/NCAR 40-Year Reanalysis Project. *Bull. Amer. Meteor. Soc.*, **77**, 437–471.
- Kistler, R., and Coauthors, 2001: The NCEP–NCAR 50-Year Reanalysis: Monthly means CD-ROM and documentation. *Bull. Amer. Meteor. Soc.*, **82**, 247–267.
- Knutson, T. R., and K. M. Weickmann, 1987: 30–60 day atmospheric oscillations: Composite life cycles of convection and circulation anomalies. *Mon. Wea. Rev.*, **115**, 1407–1436.
- Lau, K.-M., and P. H. Chan, 1985: Aspects of the 40–50 day oscillation during the northern winter as inferred from outgoing longwave radiation. *Mon. Wea. Rev.*, **113**, 1889–1909.
- Liebmann, B., and C. A. Smith, 1996: Description of a complete (interpolated) outgoing longwave radiation dataset. *Bull. Amer. Meteor. Soc.*, **77**, 1275–1277.
- Madden, R. A., and P. R. Julian, 1972: Description of global-scale circulation cells in the tropics with a 40–50 day period. *J. Atmos. Sci.*, **29**, 1109–1123.
- Maharaj, E. A., and M. C. Wheeler, 2005: Forecasting an index of the Madden–Julian oscillation. *Int. J. Climatol.*, **25**, 1611–1618.
- Matthews, A. J., 2008: Primary and successive events in the Madden–Julian oscillation. *Quart. J. Roy. Meteor. Soc.*, **134**, 439–453.
- , and G. N. Kiladis, 1999: The tropical–extratropical interaction between high-frequency transients and the Madden–Julian oscillation. *Mon. Wea. Rev.*, **127**, 661–677.
- , B. J. Hoskins, and M. Masutani, 2004: The global response to tropical heating in the Madden–Julian oscillation during northern winter. *Quart. J. Roy. Meteor. Soc.*, **130**, 1991–2011.
- Meinke, H., and R. C. Stone, 2005: Seasonal and inter-annual climate forecasting: The new tool for increasing preparedness to climate variability and change in agricultural planning and operations. *Climatic Change*, **70**, 221–253.
- Mills, G. A., G. Weymouth, D. Jones, E. E. Ebert, M. Manton, J. Lorkin, and J. Kelly, 1997: A national objective daily rainfall analysis system. Australian Bureau of Meteorology BMRC Techniques Development Rep. 1, 30 pp.
- Pohl, B., Y. Richard, and N. Fauchereau, 2007: Influence of the Madden–Julian oscillation on southern African summer rainfall. *J. Climate*, **20**, 4227–4242.
- Salby, M. L., and H. H. Hendon, 1994: Intraseasonal behavior of clouds, temperature, and motion in the tropics. *J. Atmos. Sci.*, **51**, 2207–2224.

- Schubert, S., R. Dole, H. van den Dool, M. Suarez, and D. Waliser, 2002: Prospects for improved forecasts of weather and short-term climate variability on subseasonal (2-week to 2-month) time scales. NASA Tech. Rep. NASA/TM-2002-104606, Vol. 23, 171 pp.
- Stone, R. C., and G. M. McKeon, 1993: Prospects for using weather prediction to reduce pasture establishment risk. *Trop. Grassl.*, **27**, 406–413.
- Stringer, R. K., 1992: Effects of the 40 to 50 day oscillation on Darwin rainfall. M.S. thesis, Department of Mathematics, Monash University, 132 pp.
- Tapp, R. G., and S. L. Barrell, 1984: The north-west Australian cloud band: Climatology, characteristics and factors associated with development. *J. Climatol.*, **4**, 411–424.
- Ting, M., and P. D. Sardeshmukh, 1993: Factors determining the extratropical response to equatorial diabatic heating anomalies. *J. Atmos. Sci.*, **50**, 907–918.
- Waliser, D., 2005: Predictability and forecasting. *Intraseasonal Variability in the Atmosphere-Ocean Climate System*, W. K. M. Lau and D. E. Waliser, Eds., Springer-Verlag, 389–423.
- Webster, P. J., and C. Hoyos, 2004: Prediction of monsoon rainfall and river discharge on 15–30-day time scales. *Bull. Amer. Meteor. Soc.*, **85**, 1745–1765.
- , V. O. Magana, T. N. Palmer, J. Shukla, R. A. Tomas, M. Yanai, and T. Yasunari, 1998: Monsoons: Processes, predictability, and the prospects for prediction. *J. Geophys. Res.*, **103**, 14 451–14 520.
- Weickmann, K. M., G. R. Lussky, and J. E. Kutzbach, 1985: Intraseasonal (30–60 day) fluctuations of outgoing longwave radiation and 250 mb streamfunction during northern winter. *Mon. Wea. Rev.*, **113**, 941–961.
- Wheeler, M. C., and H. H. Hendon, 2004: An all-season real-time multivariate MJO index: Development of an index for monitoring and prediction. *Mon. Wea. Rev.*, **132**, 1917–1932.
- , and J. L. McBride, 2005: Australian–Indonesian monsoon. *Intraseasonal Variability in the Atmosphere-Ocean Climate System*, W. K. M. Lau and D. E. Waliser, Eds., Springer-Verlag, 125–173.
- Wilks, D. S., 2006: *Statistical Methods in the Atmospheric Sciences*. Academic Press, 648 pp.
- Zhang, C., 2005: Madden-Julian oscillation. *Rev. Geophys.*, **43**, RG2003, doi:10.1029/2004RG000158.
- Zhao, S., and G. A. Mills, 1991: A study of a monsoon depression bringing record rainfall over Australia. Part II: Synoptic–diagnostic description. *Mon. Wea. Rev.*, **119**, 2074–2094.